Estimating the In Situ Stratification via Remotely Sensed Internal Wave Speeds

CHUFAN FANG,[a] ALEXANDRA J. SIMPSON,[b] JAMES A. LERCZAK,[c] AND MERRICK C. HALLER[a]

[a] *School of Civil and Construction Engineering, Oregon State University, Corvallis, Oregon*
[b] *Coastal and Hydraulics Laboratory, U.S. Army Engineer Research and Development Center, Field Research Facility, Duck, North Carolina*
[c] *College of Earth, Ocean, and Atmospheric Sciences, Oregon State University, Corvallis, Oregon*

(Manuscript received 5 January 2024, in final form 30 July 2024, accepted 23 August 2024)

ABSTRACT: This work tests a methodology for estimating the ocean stratification gradient using remotely sensed, high temporal and spatial resolution field measurements of internal wave propagation speeds. The internal wave (IW) speeds were calculated from IW tracks observed using a shore-based, X-band marine radar deployed at a field site on the south-central coast of California. An inverse model, based on the work of Kar and Guha, utilizes the linear internal wave dispersion relation, assuming a constant vertical density gradient is the basis for the inverse model. This allows the vertical gradient of density to be expressed as a function of the internal wave phase speed, local water depth, and a background average density. The inputs to the algorithm are the known cross-shore bathymetry, the background ocean density, and the remotely sensed cross-shore profiles of IW speed. The estimated density gradients are then compared to the synchronously measured vertical density profiles collected from an in situ instrument array. The results show a very good agreement offshore in deeper water (~50–30 m) but more significant discrepancies in shallow water (20–10 m) closer to shore. In addition, a sensitivity analysis is conducted that relates errors in measured speeds to errors in the estimated density gradients.

SIGNIFICANCE STATEMENT: The propagation speed of ocean internal waves inherently depends on the vertical structure of the water density, which is termed stratification. In this work, we evaluate and test with real field observations a technique to infer the ocean density stratification from internal wave propagation speeds collected from remote sensing images. Such methods offer a way to monitor ocean stratification without the need for extensive in situ measurements.

KEYWORDS: Internal waves; Radars/Radar observations; Inverse methods

1. Introduction

Ocean stratification (i.e., the ocean density field) plays a critical role in underwater acoustic transmission and can suppress vertical mixing and the vertical transport of nutrients. The stratification structure, where generally less dense water dwells above denser water, is important to ocean dynamics and global ocean modeling and is also reflective of the ocean heat budget through its dependence on temperature. Continual monitoring of stratification (or any water column parameter) at global scale is presently still a significant challenge, even with all the recent advances in ocean gliders, profiling floats, and satellite observing systems (Zhao 2016).

Early on, ocean acoustic tomography was proposed by Munk and Worcester (1976) to monitor the warming of the global ocean via the relationship between ocean sound speeds and temperature. Shortly after that, Mollo-Christensen and Mascarenhas (1979) argued that the then nascent satellite systems (Landsat) could be used to track internal wave (IW) speeds, which could then be related to the density field through inverse models of internal wave dispersion. Since then, several of these methods for estimating stratification parameters from observations of internal wave speeds have been developed, including some limited testing and verification with real data.

The published inverse models for estimating ocean stratification properties from remotely sensed observations of internal waves have been fairly simplified, for the most part. This is partly a consequence of the results of Jones (1995) who demonstrated the challenge of estimating unconstrained vertical profiles of the buoyancy frequency from the local IW speed. To do so, the ambient IW motion needs to be measured in both time and space. They proposed a Fourier transform method applied to the two-dimensional spatial (horizontal) and temporal domains. However, an unrealistic amount of remote sensing data was required [$O(100)$ km^2 for durations of $O(10)$ h] in order to make accurate estimates with this method.

Alternatively, a more simplified approach was taken by Porter and Thompson (1999) who based their inverse model on the linearized, two-layer constant density solution for internal wave dispersion (hereafter referred to as "two-layer model"). They successfully estimated the density of the upper mixed layer based on the distance between two IW packets in a single satellite synthetic aperture radar (SAR) image from the New York Bight region under the assumption that the two packets were generated one tidal cycle apart. Similarly, Li et al. (2000) used a single SAR image (*RADARSAT-1*) from the Middle Atlantic Bight and a two-layer model to estimate the upper-layer thickness. Stratification parameters

Corresponding author: Chufan Fang, fangchu@oregonstate.edu

DOI: 10.1175/JTECH-D-24-0001.1

needed in the calculation were from a CTD dataset collected in the same month of the previous year as the satellite observations, and for validation, they used climatology data for the mixed layer depth. Zhao et al. (2004) also used a two-layer model and a single *RADARSAT-1* image to estimate the layer densities at a site in the northeastern South China Sea with comparison to a single vertical density profile measured concurrently in situ.

All the two-layer inverse models require simplifying assumptions of some kind, some of which are poorly constrained. For example, as noted by Liu et al. (2014), it is difficult to estimate IW phase speed via satellite images with revisit times on the order of a tidal cycle (or longer). To do so requires knowing the duration of time between generation events, which is most frequently simply assumed to be the semidiurnal tidal period. As such, the observed speeds are inherently averaged over the spacing between observed IWs, which are distances of $O(10)$ km. In addition, the assumption of one IW per tidal cycle can fail in places, as McSweeney et al. (2020) demonstrated the presence of two IW packets per tidal cycle on the south-central coast of California.

The two-layer inverse model of Porter and Thompson (1999) also assumes that the density of the bottom layer can be taken from climatology data and that the upper-layer depth is spatially constant and follows directly from the shoreward limit of observed IWs. In their case, they argued that the IWs dissipate and are no longer visible in the images where the upper and lower layers have equal thickness. Hence, the total depth H at the shoreward propagation limit fixes the upper-layer thickness ($H/2$) and the inverse model then uses the observed speed to determine the spatially constant upper-layer density.

The two-layer inverse method of Zhao et al. (2004) is similar, though with the assumption of polarity reversal where the two-layer thicknesses are equal in order to estimate the density difference between the layers. The assumption of fixed upper-layer depth (i.e., depth of the mixed layer) is likely reasonable according to field studies (Liu et al. 1998; Orr and Mignerey 2003); however, identifying the shoreward limit of IW propagation from a single image is problematic and does not distinguish between the limit of shoreward propagation versus the occurrence of poor imaging conditions. In practice, the fixing of the upper-layer depth solely determines the solution.

In summary, in these previous works on inverse modeling, the number of estimated IW speeds and the availability of in situ stratification data for verification of the inverse model estimates were rather limited. In many cases, only a single satellite image is used (Porter and Thompson 1999; Li et al. 2000) or concurrent in situ measurements were not available (Mollo-Christensen and Mascarenhas 1979; Li et al. 2000; Liu et al. 2014; Kar and Guha 2020). Remote sensing technologies that can make more frequent IW observations ought to lead to improvements in the inverse modeling and will not require an assumption on the IW period. For example, Liu et al. (2014) used tandem SAR satellites that capture the same IWs in two images collected 30 min apart, thus ensuring that the speed information comes from the same IW packet and reducing the spatial averaging to 3–4 km. In their work, they did not conduct inverse modeling, but they presented speeds from tandem observations of 13 internal waves shoaling from depths of 4000–100 m and noted good agreement between the observed IW speeds and predictions from the Taylor–Goldstein equation. For the calculations, they employed monthly stratification profiles from a global database and neglected the effects of rotation and background currents. Finally, Celona et al. (2021) demonstrated speed maps of four internal tide bores in depths of ~35–25 m derived from a continuously sampling shore-based marine radar.

The previous inverse models discussed above stand in contrast to the recent work of Kar and Guha (2020), who instead assume either one-, two-, or three-layer constant density gradient and internal plane waves propagating in the vertical plane. Those authors used numerical IW simulations from a linear plane wave IW solver with a Gaussian topography as well as an idealized version of the topography at the Strait of Gibraltar. Like Jones (1995), they used a Fourier technique and extracted frequencies and wavenumbers from the simulated data to estimate one, two, and three continuously stratified layers with some success. However, the question remains of how to obtain such high-resolution data in practice.

In the present work, we utilize shore-based radar remote sensing observations of the surface manifestation of IW propagation across the inner shelf of south-central California. Specifically, we utilize a dataset of cross-shore speed profiles of seven internal waves that were extracted using a tracking technique developed and documented in Simpson et al. (2024). From data collected over several weeks, we have selected a set of seven speed profiles based on imaging quality and total cross-shore extent. The use of shore-based radar allows continuous tracking of the IW speeds and directions across the inner shelf at high spatiotemporal resolution [$O(1)$ m and $O(1)$ min] over a footprint of several kilometers offshore. Hence, individual waves can be followed as they propagate toward shore. The observations track the IW speeds as they propagated across the inner shelf, over a distance of about 6 km, from a water depth of 50 m to about 9 m. Each IW has been tracked in the radar image sequences for several hours.

In addition, we have in situ stratification data that are collocated and synchronous with the radar observations. An analysis of the in situ dataset was previously published by McSweeney et al. (2020) and included identification of the arrivals of leading internal waves at each mooring and a comparison of observed versus modeled IW speeds.

In section 2, we apply the inverse model of Kar and Guha (2020) to the observed IW speeds. Specifically, we utilize the one-layer uniform stratification model, i.e., the vertical density gradient is assumed locally constant but allowed to vary in the cross-shore. The choice of a uniform stratification model for IW dispersion is shown to compare well to the in situ stratification data. Then, from the inverse model, the cross-shore varying stratification gradient is estimated from the observed cross-shore IW speed profiles. We also examine the sensitivity of this inverse model to errors in the measured phase speeds. In section 3, we demonstrate the ability of the inverse modeling methodology to reconstruct the density field and compare the results to the in situ measurements and

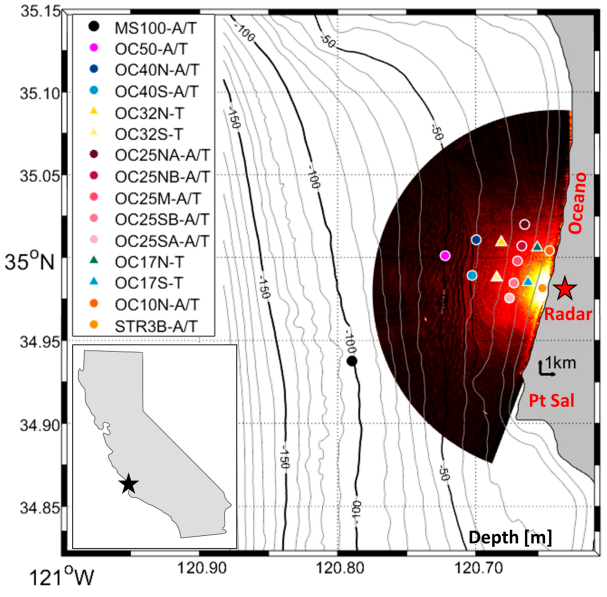

FIG. 1. Map of mooring deployment during the 2017 ISDE. Radar was located at GD. Radar color indicates relative backscatter intensity; several IWs can be seen as linear features between OC50 and OC32.

discuss the increased errors in depths of 20 m and less. Finally, section 4 summarizes the work.

2. Methodology

a. Dataset

The Inner-Shelf Dynamics Experiment (ISDE; Kumar et al. 2021) was conducted in the fall of 2017 along the south-central coast of California at Point Sal and aimed to study inner-shelf processes and their interconnections using a wide range of in situ, remote sensing, and modeling techniques. In the present work, we have utilized a subset of the array of moorings that was deployed offshore of Oceano, California, as shown in Fig. 1, and X-band radar observations recorded from a shore-based tower at Guadalupe Dunes (GD), California, as shown in Fig. 2. The moorings were located in a range of depths from 100 to 9 m and recorded the temperature profiles at 1-min intervals from early September to early November. Previous data analysis demonstrated that at OC50, the salinity only varied from 33.25 to 33.58 g kg^{-1}; therefore, density was fully determined by the measured temperature and pressure only, which was subsequently interpolated onto vertical profiles (McSweeney et al. 2020). We choose the six moorings OC50, OC40S, OC32S, OC25SB, OC17S, and STR3B, which represent the southern axis of the cross-shore array that was analyzed in McSweeney et al. (2020) and have good overlap with the X-band radar image footprint. Depth and cross-shore location of moorings are listed in Table 1.

Radar images of IWs were collected concurrently with the in situ measurements and were sampled with 3-m resolution in range and ~1° resolution in azimuth with an overall footprint radius of 10 km. The radar scans were collected every ~1.7 s and then averaged over 2 min to create a "wave-averaged" image, which removes the strong signatures of the surface gravity waves and enhances the visibility of longer-dwell features such as internal waves (Haller et al. 2019). The white line on the radar image in Fig. 2a represents a cross-shore transect from which the 2-min-averaged backscatter intensity was extracted to create a space–time diagram, as shown in Fig. 2b. A filtering technique was then applied to the space–time diagram to normalize the range-dependent roll-off of backscatter intensity (Simpson et al. 2024). The bright curvilinear features in the diagram represent the trajectories of internal bores as they propagate cross-shore over time. By

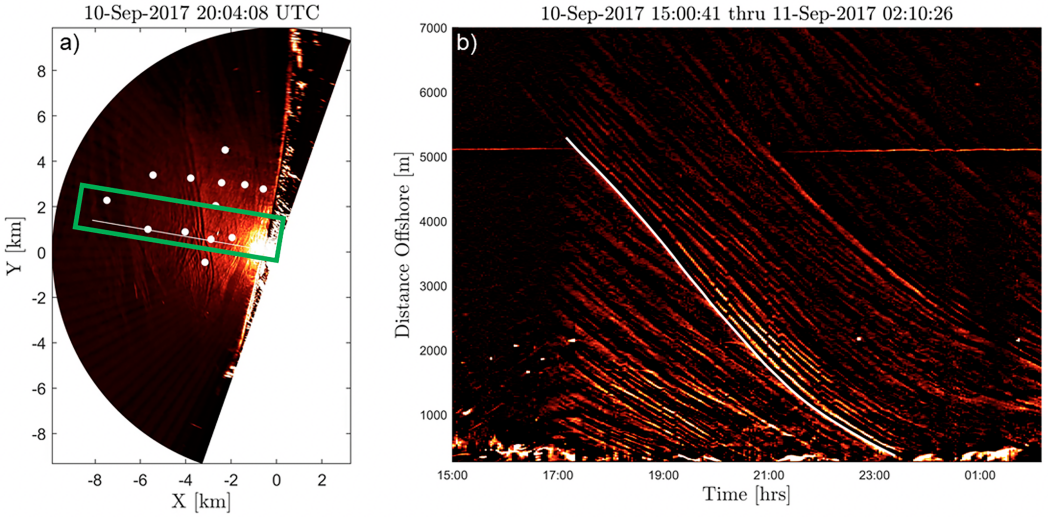

FIG. 2. (a) Single radar image. Circles indicate in situ mooring locations, and white line shows transect extracted for the space–time diagram. Moorings used for the following analysis are boxed in green. (b) Space–time diagram extracted from the time-averaged radar images. White line indicates the track of the leading bore. Figures from Simpson et al. (2024).

TABLE 1. Depth and cross-shore distance of each mooring site. The distance is measured as the along-transect distance to the mean shoreline identified in the radar imagery.

Mooring	OC50	OC40S	OC32S	OC25SB	OC17S	STR3B
Cross-shore distance (m)	6592	4852	3640	2712	1451	694
Depth (m)	49.2	40.8	32.2	24.7	16.3	8.2

calculating the local slopes, the cross-shore variation of IW propagation speeds are obtained, and we utilize the speeds of the leading bores from a number of IW packets. To account for the oblique wave incidence, the transect is chosen to align roughly with the wave direction, and the calculated speed is corrected using the wave incidence angle also determined from the radar observations. Wave incident angles yield up to 3% offset in speed values and are considered insignificant. The reader is advised to see Simpson et al. (2024) for further details on the IW tracking methodology. At each in situ mooring location, density profiles were sampled at 1-min intervals. The observed wave arrivals are used to determine the prearrival stratification conditions. Density profiles were averaged over the 15-min window before the arrival minute. The IWs are numbered by their order of arrival (McSweeney et al. 2020).

b. *Internal wave dispersion*

We consider a continuously stratified, incompressible, and inviscid fluid. Following McSweeney et al. (2020), we also neglect the Coriolis acceleration, so the equation of the linear and hydrostatic internal wave motion (Gerkema and Zimmerman 2008) is given by

$$\frac{\partial^2 \hat{w}}{\partial z^2} + \frac{N^2}{c^2}\hat{w} = 0, \tag{1}$$

where $\hat{w}$ is the vertical structure function, with the phase speed c defined by $c = \sigma/k$; σ is the IW angular frequency; k is the horizontal wavenumber; and $N(z)$ is the buoyancy frequency that reflects the density stratification:

$$N(z) = \sqrt{-\frac{g}{\rho_0}\frac{\partial \rho(z)}{\partial z}}, \tag{2}$$

where ρ_0 is the background density that is necessarily taken to be a constant in the following linear analysis.

It should be noted that the solution of Eq. (1) has multiple modes, but only the first mode (corresponding to the largest speed) is considered in the following analysis, since the lowest mode usually dominates (Phillips 1966) and because McSweeney et al. (2020) documented that the observations from this site primarily contained mode-one IWs.

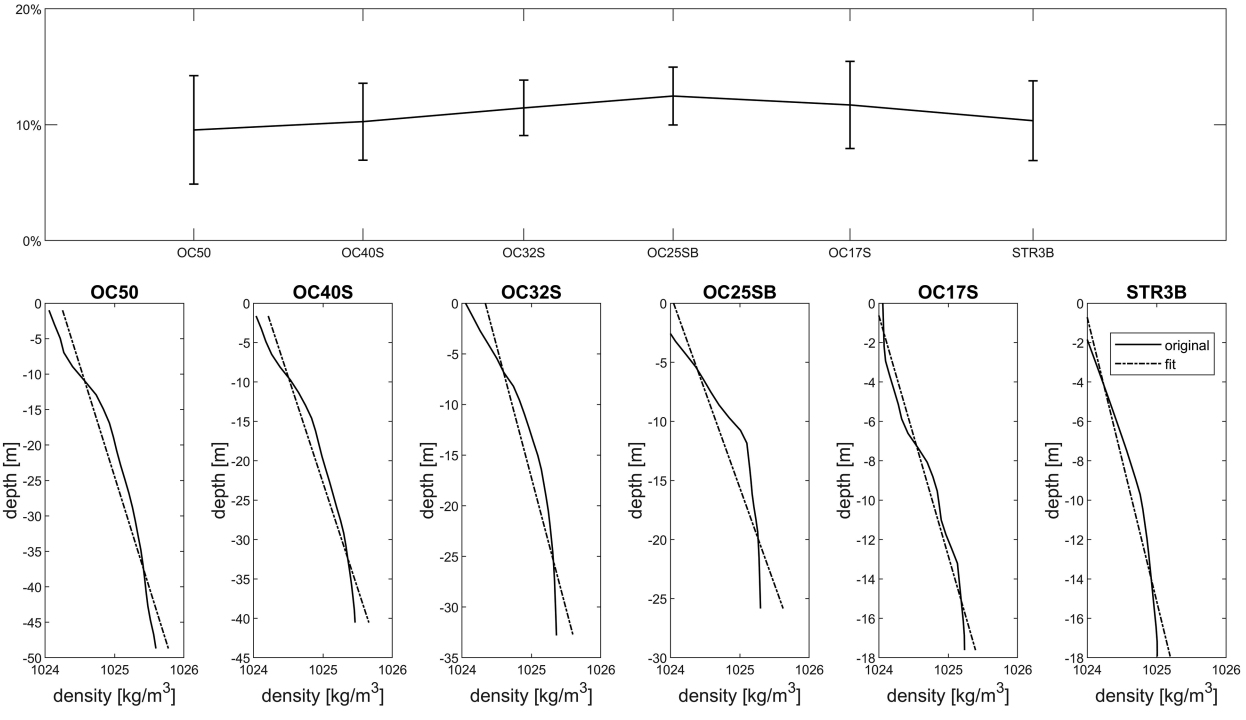

FIG. 3. (top) NRMSE [Eq. (4)] at each mooring site between the original density and linear fit profiles. Errors are averaged over seven observed waves passing through each mooring. Vertical bars represent the standard deviation of NRMSE over the set of seven IWs. (bottom) Comparison of measured density profile (solid line) to that from a linear fit (dash–dotted line) at six mooring sites for wave 18. Measured density is averaged over the 15-min prearrival time frame.

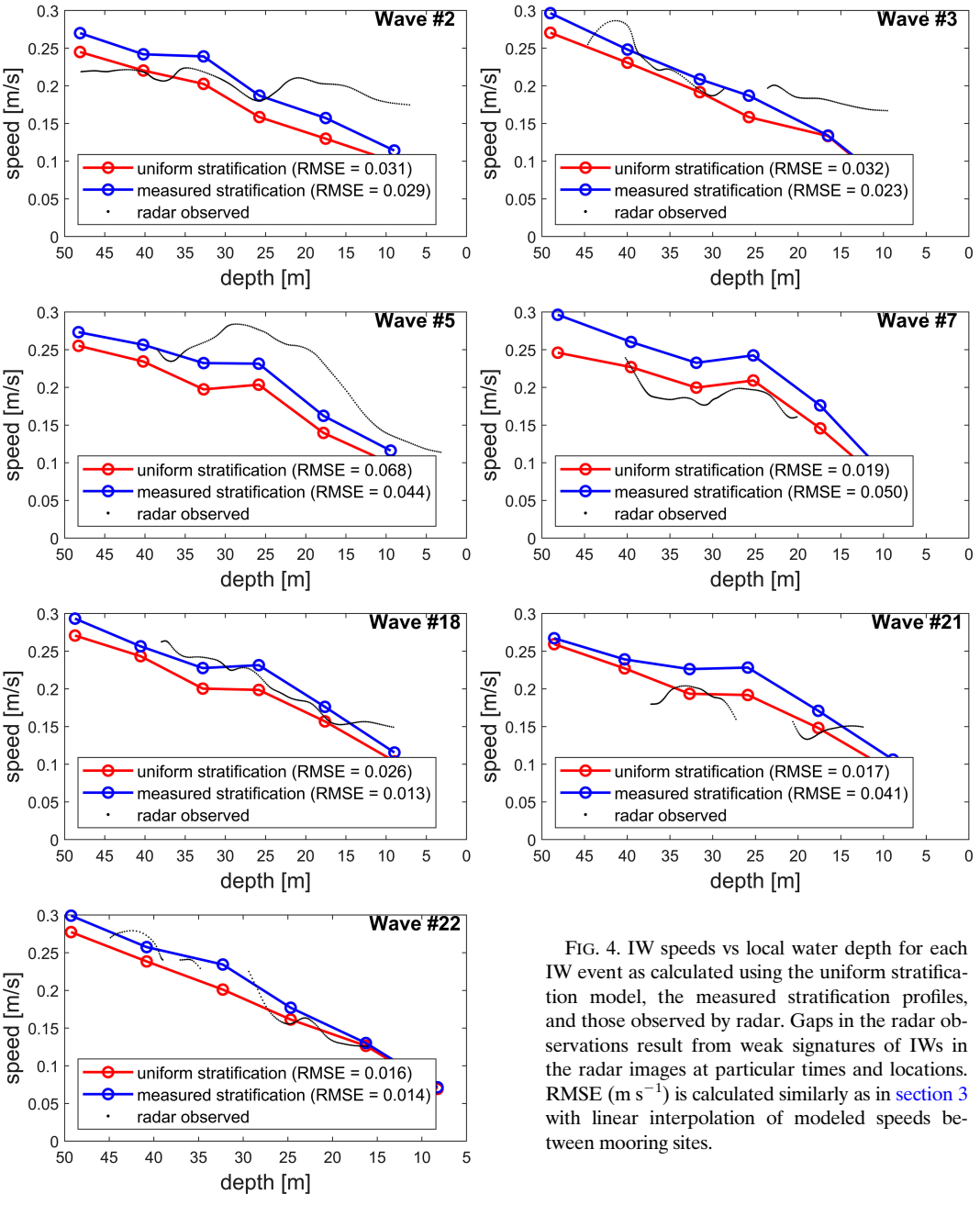

FIG. 4. IW speeds vs local water depth for each IW event as calculated using the uniform stratification model, the measured stratification profiles, and those observed by radar. Gaps in the radar observations result from weak signatures of IWs in the radar images at particular times and locations. RMSE (m s^{-1}) is calculated similarly as in section 3 with linear interpolation of modeled speeds between mooring sites.

To solve for $\hat{w}$ and c in Eq. (1) with an arbitrary density function (such as the measured density profiles), a finite difference method can be applied (Pozrikidis 1998). Alternatively, by assuming a uniform stratification, in which the vertical density gradient ($\partial\rho/\partial z$, written as ρ_z hereafter) is constant in the vertical, it follows that the buoyancy frequency N is also constant in the vertical. Thereby, Eq. (1) can be solved analytically yielding the first-mode dispersion relation for uniform stratification (Gerkema and Zimmerman 2008; Kar and Guha 2020):

$$c^2 = \frac{g(-\rho_z)h^2}{\pi^2\rho_0}, \tag{3}$$

where h is the total depth. Comparison of the IW speeds calculated by the two methods above is given in section 3a.

To justify the applicability of the uniform stratification model, first we examine the difference between the best-fit linear density profiles and the observations. Following Kar and Guha (2020), we utilize the normalized root-mean-square error, defined as

$$\mathrm{NRMSE} = \frac{\sqrt{\frac{1}{N}\sum_{i=1}^{N}(\rho_i^a - \rho_i^f)^2}}{\rho_{\max}^a - \rho_{\min}^a}, \tag{4}$$

with superscript a denoting the actual data and f as the linear fit. At each mooring location, the NRMSE is calculated and averaged over all IW prearrival cases (Fig. 3). The top panel of Fig. 3 shows the best-fit linear density profiles for an example IW (wave 18) at each mooring location compared to the observed. The bottom panel shows the NRMSE and standard deviations. The NRMSEs at the six mooring sites have an average around 10%, demonstrating that the uniform stratification decently approximates the observed density profiles.

c. Inverse model

The dispersion relation Eq. (3) shows that the IW phase speed is determined by three stratification parameters: the total depth h, vertical density gradient ρ_z, and the background density ρ_0. Inversely, observed values of the phase speed, water depth, and background density can yield the density gradient. Rearranging Eq. (3) to get the expression for the gradient,

$$\rho_z = -\frac{c^2\pi^2\rho_0}{gh^2}. \tag{5}$$

A sensitivity analysis of this equation with respect to measurement errors is given in section 3b.

3. Results

a. Forward modeling

As a first test of the inverse model using uniform stratification, we examine the forward model for IW speed. Specifically, in Fig. 4, we compare the linear IW speeds predicted by 1) the numerical solution of Eq. (1) with the measured, depth-varying density profiles, 2) dispersion relation with uniform stratification given by Eq. (3), and 3) the speeds observed by radar. Input into the uniform stratification model are the best-fit vertical gradient to the measured data at each mooring (for each prearrival window), the water depth from existing bathymetry data, and a constant background density taken from the average over all of the observed density profiles. Specifically, we use the measured density profiles of each prearrival window to integrate density across the domain and then divide by the cross-sectional domain area to find the representative background density for each IW. The calculated background density for each IW arrival does not change significantly (1024.8–1025.1 kg m^{-3}); hence, we take an average over all IWs (ρ_0 = 1025.0 kg m^{-3}) as the background density value used in all calculations.

As listed in Fig. 4, root-mean-square errors of the speeds calculated by the uniform stratification model with respect to the radar observations are calculated for each observed wave, and for most cases, the errors are between 0.02 and 0.03 m s^{-1}, which are 7%–10% of the observed speeds [$\sim O(0.3)$ m s^{-1}] and considered small. At the shallower sites, the observed speeds are higher than the speeds calculated by the uniform stratification dispersion model (e.g., wave 2). The present analysis cannot distinguish the cause of the increased error at the shallowest sites; however, one possibility is the influence of increased IW nonlinearity (see e.g., Helfrich and Melville 1986), which is not included in the IW dispersion considered here. Nonetheless, the uniform stratification speeds largely agree with the remotely sensed speeds, and the speeds calculated numerically using the observed stratification and Eq. (3) are not much different. From this, we determine that it is effective to proceed with the uniform stratification model.

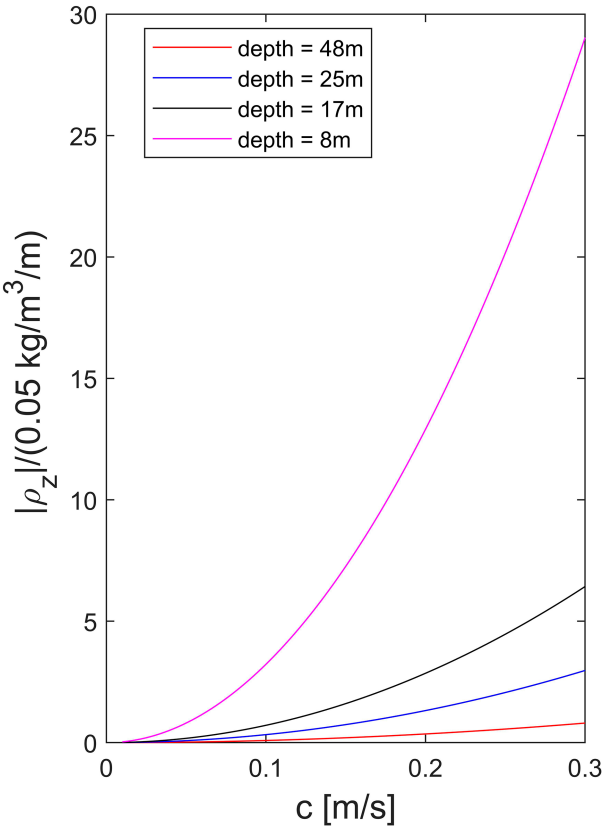

FIG. 5. Sensitivity of the inverse modeled (and normalized) density gradient magnitude $|\rho_z|'$ to the IW speed at four representative depths. Gradients are calculated by the inverse model equation [Eq. (5)]. Density gradients are normalized by 0.05 kg m^{-3} m^{-1}, which is the order of magnitude of the measured gradients (Fig. 6).

b. Sensitivity analysis

Equation (5) indicates that the calculated ρ_z depends on three arguments: c, h, and ρ_0. To evaluate how the input error from measurements influences the density gradient estimation error, we follow the method of Dalrymple et al. (1998). A similar approach can be found in Kar and Guha (2020).

Taking the total derivative of ρ_z in Eq. (6),

$$d\rho_z = (-1)\frac{2c\pi^2\rho_0}{gh^2}\,dc + (-1)\frac{c^2\pi^2}{gh^2}\,d\rho_0 + 2\frac{c^2\pi^2\rho_0}{gh^3}\,dh. \tag{6}$$

We shall take the differential terms as the local absolute error of the variables. Dividing both sides of Eq. (6) by ρ_z and rearranging,

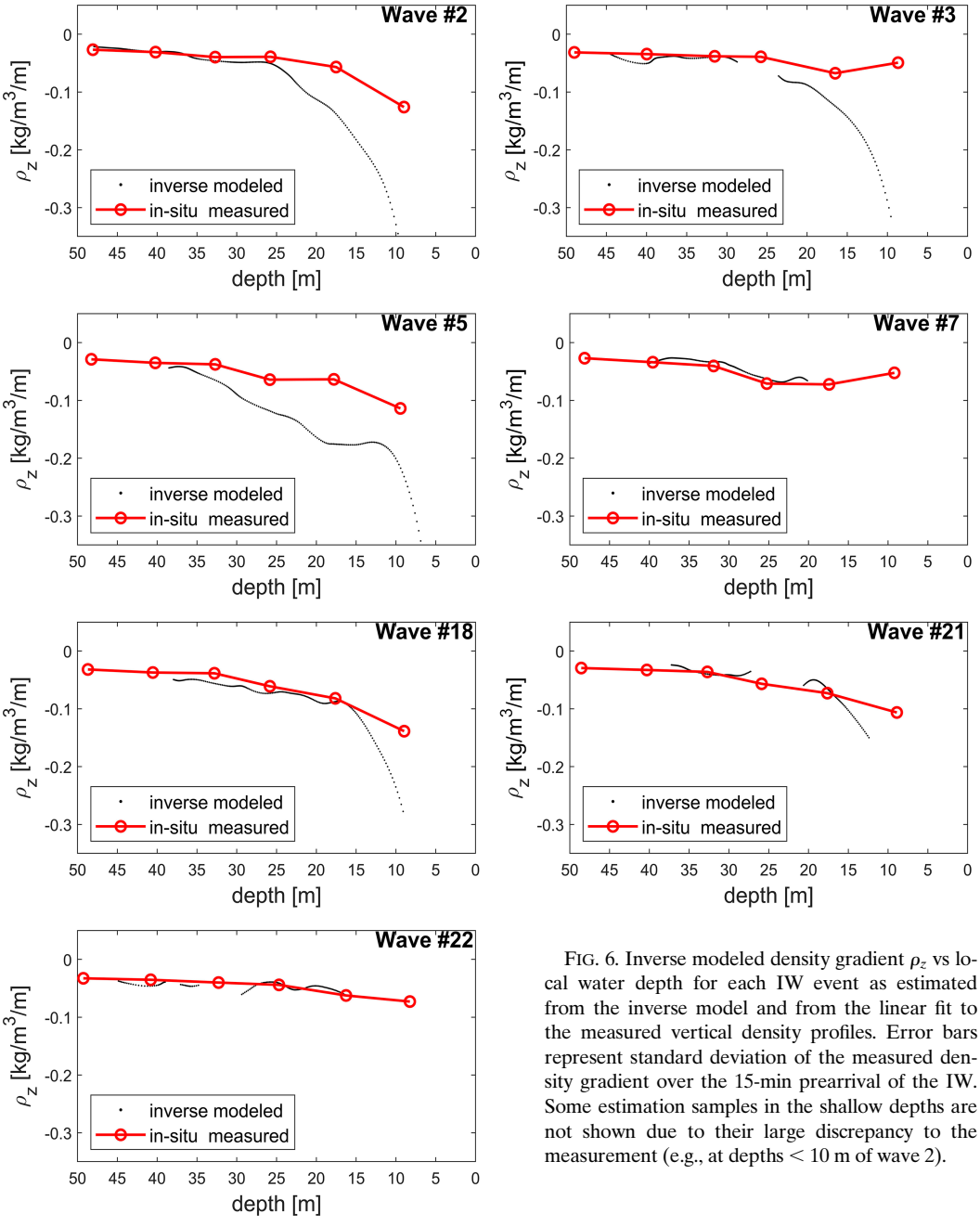

FIG. 6. Inverse modeled density gradient ρ_z vs local water depth for each IW event as estimated from the inverse model and from the linear fit to the measured vertical density profiles. Error bars represent standard deviation of the measured density gradient over the 15-min prearrival of the IW. Some estimation samples in the shallow depths are not shown due to their large discrepancy to the measurement (e.g., at depths < 10 m of wave 2).

$$\frac{d\rho_z}{\rho_z} = 2\frac{dc}{c} + \frac{d\rho_0}{\rho_0} + (-2)\frac{dh}{h}. \tag{7}$$

The terms of form dX/X (X being any of the four variables: ρ_z, c, ρ_0, or h) represent the dimensionless relative error. Coefficients of the terms on the right-hand side imply that the errors transmitted to the gradient estimate will be twice the respective measurement errors in phase speed and water depth, while errors in background density transmit at the same scale. The uncertainty of the background density is generally very small and therefore neglected; hence, we use the representative ρ_0 as stated earlier (section 3a). It should be noted that since the analysis above only considers the first-order derivative, this relation is only valid when the input error is small. It should also be noted that in shallow water, the sensitivity of $|\rho_z|$ to c increases, as illustrated in Fig. 5. This is evident by the steeper slopes for the shallower water curves, which indicates the increasing sensitivity of the vertical gradient to changes in speed and, therefore, to any speed measurement errors. Similarly, nonlinear dispersive effects in the observed speeds will lead to discrepancies in the estimated gradients.

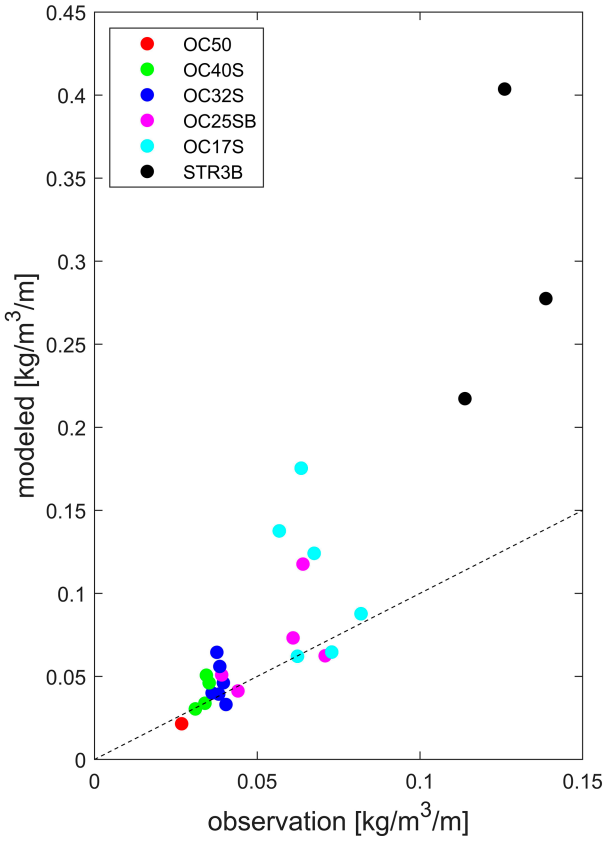

FIG. 7. Estimated density gradients vs observed. Colors indicate the different mooring site depths.

c. *Inverse modeling*

Next, we test the inverse model that estimates the spatial variability of the ocean density gradient across the continental shelf based on the observed IW speeds. The inputs to the inverse model [Eq. (5)] are the observed IW phase speeds c, total water depth h, and the background density ρ_0. Figure 6 compares the gradients estimated by the inverse model with those measured in situ for each IW and all of the data are shown as a scatterplot in Fig. 7. From these figures, we see that the inverse model is generally good, at least to water depths as shallow as 20 m. However, the errors clearly

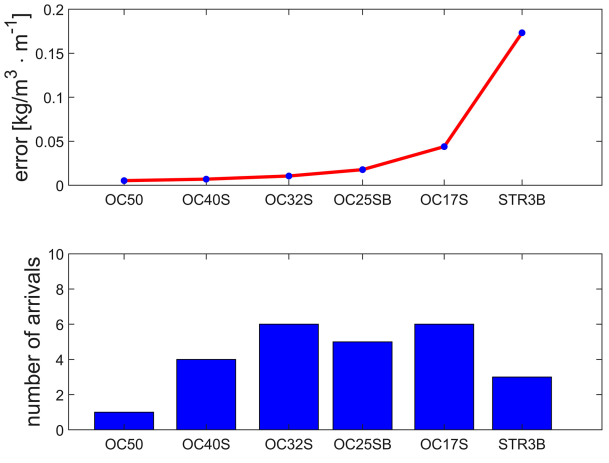

FIG. 8. (top) Estimation error of density gradient characterized by root-mean-square error. The error at each mooring site is averaged over the arrival events observed in each location. (bottom) Number of observed arrival events.

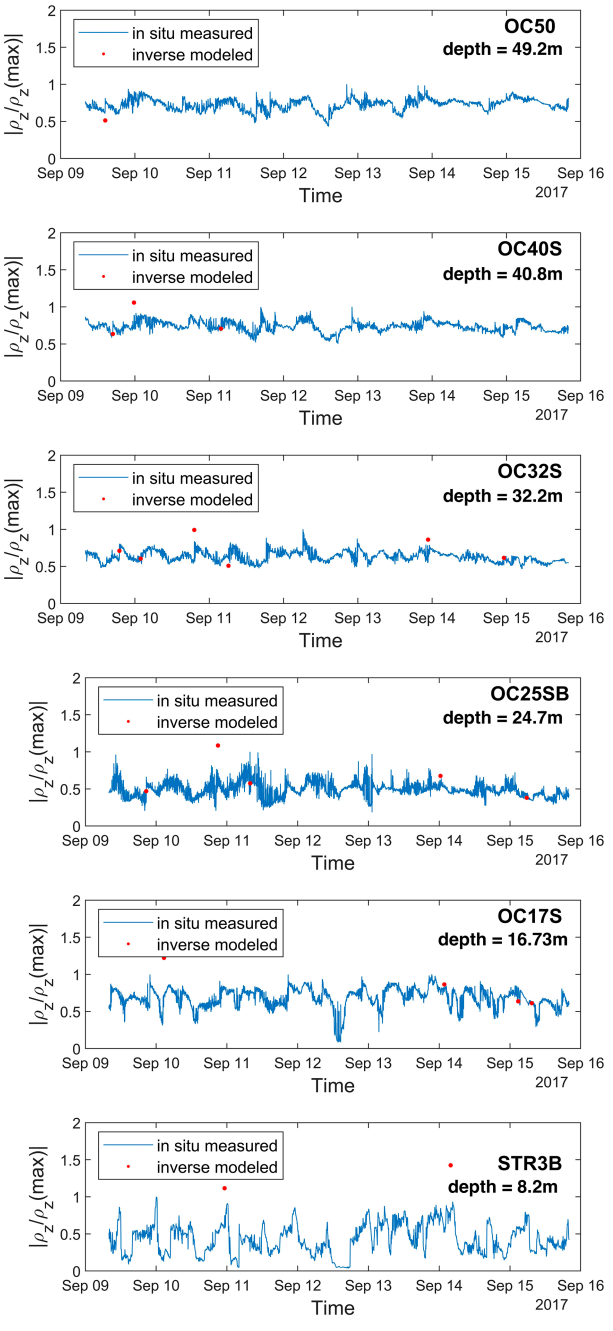

FIG. 9. Time series of gradients from fitting the in situ density (blue lines, in 1-min interval) and estimated gradients (red dots) of each arrival, at the six mooring sites. Gradients are scaled by each site's maximum fit values over the measurement time period.

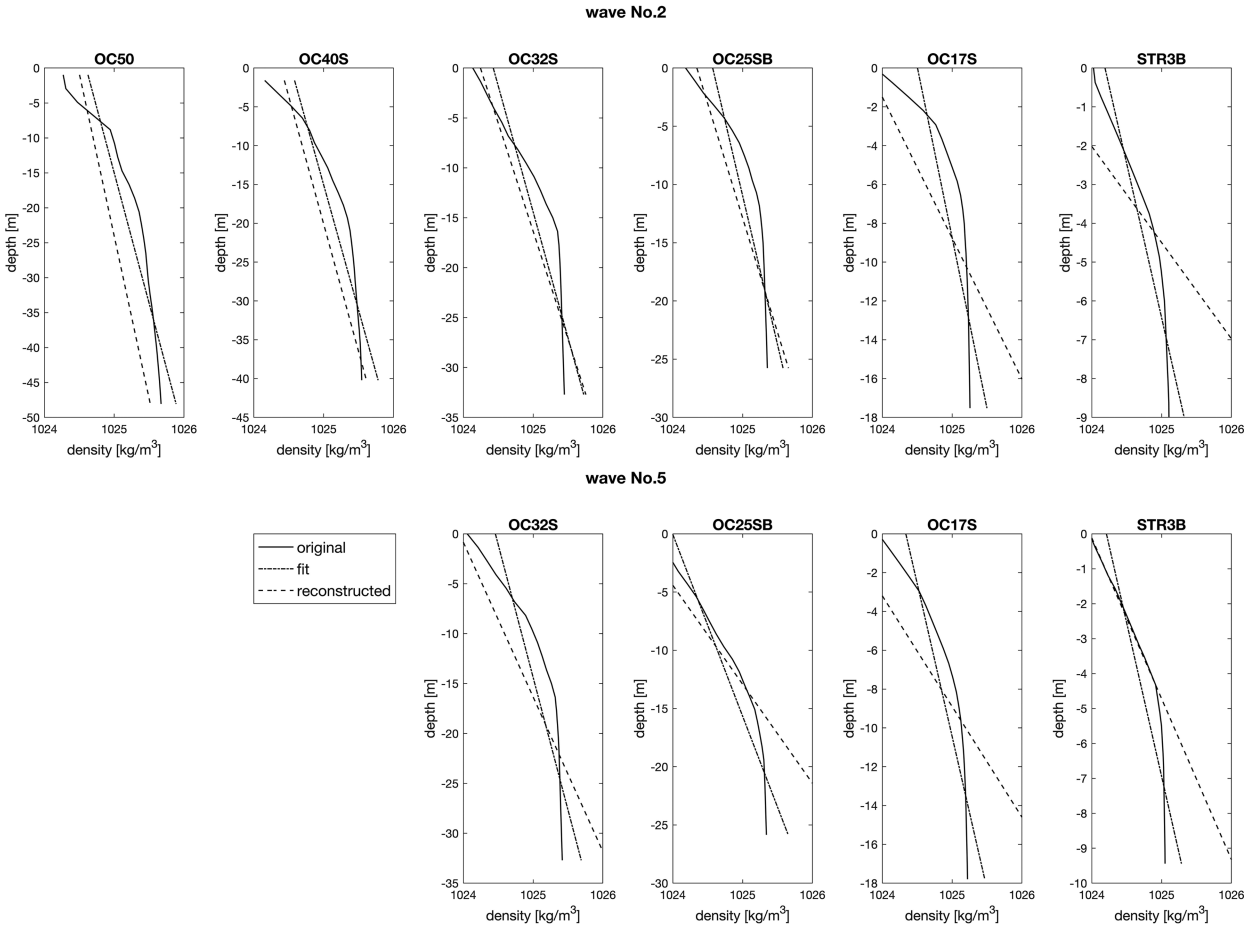

FIG. 10. Reconstructed density profiles for (top) wave 2 and (bottom) wave 5 shown as dash lines for each mooring location. Measure density profiles are shown as solid lines and linear fits to the measured profiles are shown as dash–dotted lines.

increase in shallow regions (e.g., OC17S and STR3B), which are also regions of higher-density gradients.

In Fig. 8, we quantify the estimation error of the density gradient at each mooring location by the difference between the estimation and measurement averaged over the number of events that have overlapping radar data (this is a different number of events for each location as shown in the bar plot). The figure shows a cross-shore trend in the accuracy of the inverse model with better results offshore and error increasing significantly at total depths less than 20 m, this being a result of both the increase in sensitivity to measurement errors at the shallowest sites (section 3b) and the impact of increased nonlinearity as well.

To see how well the inverse algorithm performs in the context of the overall stratification variability, we plot the time series of the observed and estimated density gradients over the 8-day window in Fig. 9. It is evident that the shallowest mooring sites exhibit the most temporal variability of the local density gradient. The time variability at the semidiurnal scale is mainly the result of the passing of the internal tidal bores, which affect the local stratification more so than the cross-shore barotropic tidal currents, as shown by McSweeney et al. (2020). Also, at the shallowest site (STR3B), where there is the most time variability, it is evident that the measured gradient was always less than any of the estimates suggesting that the chosen linear IW dispersion model is not satisfactory here. Overall, there are less inversely modeled gradients shown in this figure because of the limitations of overlap between the estimates and the mooring locations (see Fig. 6).

Finally, we compare the estimated density field and the buoyancy frequencies to the in situ measurements. First, we reconstruct the density field from the inverse model results as shown in Fig. 10. Waves 2 and 5 are chosen as there was good cross-shore coverage of the radar-estimated IW speeds. Since it is only the vertical density gradient that is estimated by the inverse model, in order to reconstruct the vertical density profile, we assume the density at mid water column at each location is equal to the background density value (therefore, both estimated and measured profiles have the same depth-averaged value). Figure 10 shows the reconstructed density, the original profile, and least squares fit data in each mooring sites.

Figure 11 compares the vertical profiles of in situ buoyancy frequency $N(z)$, the vertical mean $\overline{N}$, and standard deviation

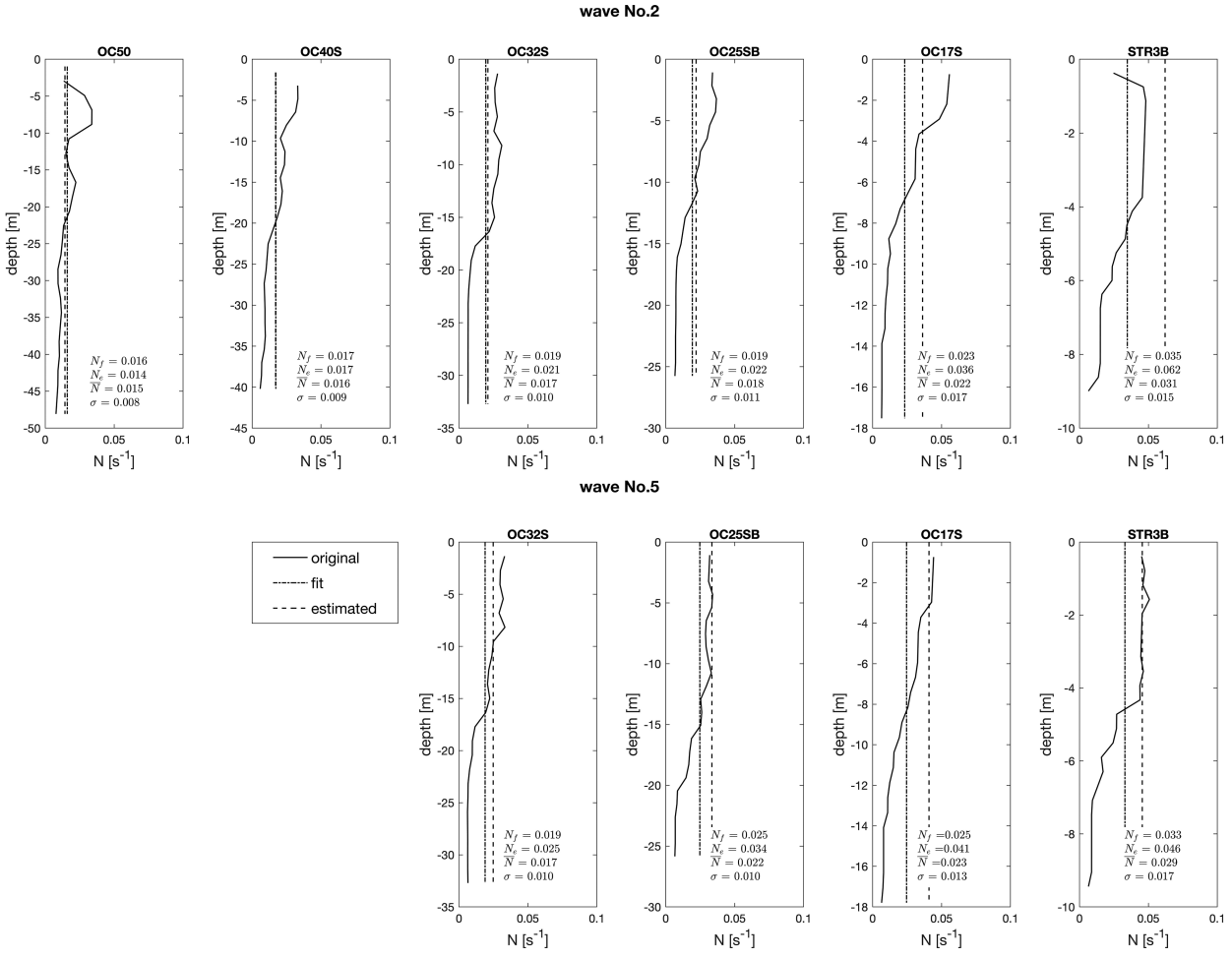

FIG. 11. Vertical profiles of buoyancy frequency at each mooring location for (top) wave 2 and (bottom) wave 5. The $N(z)$ calculated by the measured density profile is shown as solid lines. Dashed lines and dash–dotted lines show $N(z)$ calculated from fit profiles (i.e., N_f) and from the estimated density gradient (N_e), respectively.

σ all calculated from the observed density gradients [Eq. (2)], with those calculated from the best-fit ρ_z (N_f) and from the inverse estimated ρ_z (N_e). These data demonstrate that the inverse estimated buoyancy frequency matches the mean in situ value quite well, for the most part, and generally falls within the range of measured values in the vertical. Additionally, the in situ vertical profiles suggest that an assumption of a linearly varying buoyancy frequency might lead to an improved inverse model. This hypothesis is left to be tested in future work.

4. Conclusions

Through this work, we demonstrate the feasibility of monitoring the regional stratification in water depths of 20–50 m with remotely sensed internal wave speed profiles. Utilizing a set of existing marine radar measurements of IW speeds, over a distance of approximately 6 km across the inner shelf region and with a 2-min time resolution, an inverse model for estimating ocean stratification was tested. The density gradients measured in situ were reasonably characterized by a single layer of constant density gradient with the best-fit linear density profile errors around 10% on average. The results of the inverse modeling show that, where vertical density profiles are reasonably characterized by uniform stratification, they can be estimated using the observed IW speeds, known bathymetry profile, and known background density. The in situ observed vertical gradients varied from about 0.03 to 0.13 kg m^{-3} m^{-1}. Errors in the estimated gradients significantly increase in depths less than 15–20 m from 0.005 kg m^{-3} m^{-1} at the 50-m mooring to 0.2 kg m^{-3} m^{-1} at the 8-m mooring. A sensitivity analysis demonstrates the increased sensitivity of the estimated gradient to the local IW speed (and therefore to errors in observed speed) in depths less than 20 m. Finally, using the estimated density gradient, we reconstruct the full vertical density profiles and compare to observations for two IW events. Clearly, the linear IW dispersion model, based on uniform stratification and neglecting ambient currents, appears much less appropriate at depths less than 20 m. Estimated buoyancy frequencies from the inverse model

generally fall within the range of values seen in the in situ vertical profiles and match their vertical means.

Acknowledgments. We are grateful for the funding support from the Office of Naval Research under Grants N00014-15-1-2020 and N00014-15-1-2617. JAL was also supported by NSF Grant OCE-2220439. There are no conflicts of interest to declare. We thank Dr. Porter and Dr. Guha for their constructive comments that have improved the paper.

Data availability statement. The in situ data utilized in this work are archived at "Observations and Model Simulations from the Inner-Shelf Dynamics Experiment (ISDE)," https://doi.org/10.6075/J0DV1K1N. Data presenting in this paper can be immediately accessed by contacting Chufan Fang at fangchu@oregonstate.edu.

REFERENCES

Celona, S., S. T. Merrifield, T. de Paolo, N. Kaslan, T. Cook, E. J. Terrill, and J. A. Colosi, 2021: Automated detection, classification, and tracking of internal wave signatures using X-band radar in the inner shelf. *J. Atmos. Oceanic Technol.*, **38**, 789–803, https://doi.org/10.1175/JTECH-D-20-0129.1.

Dalrymple, R. A., A. B. Kennedy, J. T. Kirby, and Q. Chen, 1998: Determining depth from remotely-sensed images. *Coastal Engineering 1998*, American Society of Civil Engineers, 2395–2408, https://doi.org/10.1061/9780784404119.180.

Gerkema, T., and J. T. F. Zimmerman, 2008: An introduction to internal waves. Royal NIOZ Lecture Notes, 207 pp., https://core.ac.uk/download/pdf/92866879.pdf.

Haller, M. C., D. A. Honegger, R. Pittman, A. O'Dea, and A. Simpson, 2019: Real-time marine radar observations of nearshore waves and flow structures from shore-based towers. *2019 IEEE/OES 12th Current, Waves and Turbulence Measurement (CWTM)*, San Diego, CA, Institute of Electrical and Electronics Engineers, 1–7, https://doi.org/10.1109/CWTM43797.2019.8955152.

Helfrich, K. R., and W. K. Melville, 1986: On long nonlinear internal waves over slope-shelf topography. *J. Fluid Mech.*, **167**, 285–308, https://doi.org/10.1017/S0022112086002823.

Jones, R. M., 1995: On using ambient internal waves to monitor Brunt-Väisälä frequency. *J. Geophys. Res.*, **100**, 11 005–11 011, https://doi.org/10.1029/95JC00139.

Kar, S., and A. Guha, 2020: An inverse technique for reconstructing ocean's density stratification from surface data. *Ocean Modell.*, **147**, 101561, https://doi.org/10.1016/j.ocemod.2019.101561.

Kumar, N., and Coauthors, 2021: The inner-shelf dynamics experiment. *Bull. Amer. Meteor. Soc.*, **102**, E1033–E1063, https://doi.org/10.1175/BAMS-D-19-0281.1.

Li, X., P. Clemente-Colon, and K. S. Friedman, 2000: Estimating oceanic mixed-layer depth from internal wave evolution observed from Radarsat-1 SAR. *Johns Hopkins APL Tech. Dig.*, **21**, 130–135.

Liu, A. K., Y. S. Chang, M.-K. Hsu, and N. K. Liang, 1998: Evolution of nonlinear internal waves in the East and South China Seas. *J. Geophys. Res.*, **103**, 7995–8008, https://doi.org/10.1029/97JC01918.

Liu, B., H. Yang, Z. Zhao, and X. Li, 2014: Internal solitary wave propagation observed by tandem satellites. *Geophys. Res. Lett.*, **41**, 2077–2085, https://doi.org/10.1002/2014GL059281.

McSweeney, J. M., and Coauthors, 2020: Observations of shoaling nonlinear internal bores across the central California inner shelf. *J. Phys. Oceanogr.*, **50**, 111–132, https://doi.org/10.1175/JPO-D-19-0125.1.

Mollo-Christensen, E., and A. S. Mascarenhas Jr., 1979: Heat storage in the oceanic upper mixed layer inferred from Landsat data. *Science*, **203**, 653–654, https://doi.org/10.1126/science.203.4381.653.

Munk, W., and P. Worcester, 1976: Monitoring the ocean acoustically. *Science, Technology and the Modern Navy; Thirtieth Anniversary 1946-1976*, E. I. Salkovitz, Ed., Office of Naval Research, 497–508.

Orr, M. H., and P. C. Mignerey, 2003: Nonlinear internal waves in the South China Sea: Observation of the conversion of depression internal waves to elevation internal waves. *J. Geophys. Res.*, **108**, 3064, https://doi.org/10.1029/2001JC001163.

Phillips, O. M., 1966: *The Dynamics of the Upper Ocean*. Cambridge University Press, 261 pp.

Porter, D. L., and D. R. Thompson, 1999: Continental shelf parameters inferred from SAR internal wave observations. *J. Atmos. Oceanic Technol.*, **16**, 475–487, https://doi.org/10.1175/1520-0426(1999)016<0475:CSPIFS>2.0.CO;2.

Pozrikidis, C., 1998: *Numerical Computation in Science and Engineering*. Oxford University Press, 1280 pp.

Simpson, A. J., J. M. McSweeney, J. A. Lerczak, and M. C. Haller, 2024: Event-scale internal tide variability via X-band marine radar. arXiv, 2404.18218v1, https://doi.org/10.48550/arXiv.2404.18218.

Zhao, Z., 2016: Using CryoSat-2 altimeter data to evaluate M_2 internal tides observed from multisatellite altimetry. *J. Geophys. Res. Oceans*, **121**, 5164–5180, https://doi.org/10.1002/2016JC011805.

——, V. Klemas, Q. Zheng, X. Li, and X.-H. Yan, 2004: Estimating parameters of a two-layer stratified ocean from polarity conversion of internal solitary waves observed in satellite SAR images. *Remote Sens. Environ.*, **92**, 276–287, https://doi.org/10.1016/j.rse.2004.05.014.